Research
Medical Engineering—Article

MXene Hydrogel Microneedles with Nitric Oxide and HIF-1α Plasmid Controllable Releasing for Wound Healing

Wanchuan Ding [a], Xiangyi Wu [a], Yi Cheng [a], Ling Lu [b,*], Weijian Sun [c,*], Yuanjin Zhao [a,b,c,*]

[a] Department of Rheumatology and Immunology, Nanjing Drum Tower Hospital, School of Biological Science and Medical Engineering, Southeast University, Nanjing 210096, China
[b] Department of Otolaryngology Head and Neck Surgery, Zhongda Hospital, Southeast University, Nanjing 210096, China
[c] Department of Gastrointestinal Surgery, The First Affiliated Hospital of Wenzhou Medical University, Wenzhou 325035, China

ABSTRACT

Microneedle technology is valuable in wound treatment. Current studies focus on optimizing the function of microneedles and screening for effective encapsulated actives. Herein, we develop innovative MXene hydrogel microneedles with nitric oxide (NO) and hypoxia-inducible factor-1α (HIF-1α) plasmid controllable release for diabetic wound treatment. These microneedles consist of gelatin coupled with tert-butyl nitrite (Gel-SNO) polymers obtained by conjugating the –SNO group on the gelatin side chain, therefore, NO can be generated and released under near-infrared (NIR) light irradiation owing to the thermal effect. Simultaneously, by harnessing the enhanced photothermal conversion efficiency of the MXene additive, the microneedle patch can quickly dissolve and liberate the enclosed HIF-1α plasmid nanoparticles into the dermis when exposed to NIR radiation. The released NO effectively reduced the inflammatory response and released HIF-1α plasmid induced neovascularization. Thus, *in vivo* experiments showed that these microneedles could accelerate wound closure by alleviating inflammation, and promoting re-epithelialization and angiogenesis. These results indicated the potential value of MXene hydrogel microneedles in wound healing and other related biomedical fields.
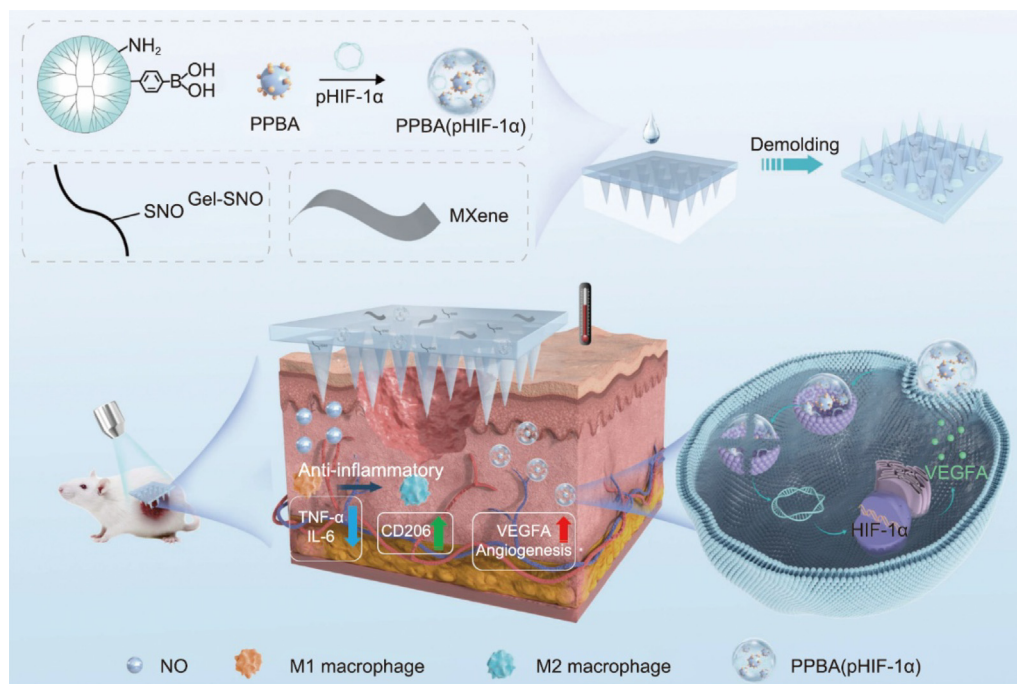
1. Introduction

Persistent non-healing wounds represent a substantial and common complication of diabetes, placing a considerable strain on the healthcare system [1–4]. Generally, proinflammatory cytokine overexpression and compromised angiogenesis occur in these wounds, resulting in impaired extracellular matrix formation, hindered re-epithelialization, and delayed wound healing [5–12]. To address these challenges, various hydrogel patches have been developed to deliver therapeutic agents, such as oxygen, living cells, and growth factors, for diabetic wound treatment [13–19]. Although these hydrogel patches involve many processes, they usually have substantial limitations in treating diabetic wounds [20–22]. For example, it is difficult for traditional hydrogel patches to penetrate the skin barrier for active delivery, which diminishes their therapeutic efficacy. In addition, existing patch treatments primarily provide symptomatic relief rather than addressing the

underlying pathological mechanisms, such as prolonged inflammation and inadequate angiogenesis. Therefore, there is a pressing need for innovative strategies with anti-inflammatory and pro-angiogenic properties to effectively manage chronic diabetic wounds.

In this paper, we proposed novel MXene hydrogel microneedles (MNs) to controllably deliver nitric oxide (NO) and hypoxia-inducible factor-1α (HIF-1α) plasmid nanoparticles for diabetic wound treatment, as illustrated in Fig. 1. MNs are an alternative for transdermal delivery and can penetrate the skin in a painless, minimally invasive, and noninfectious way [23–26]. They can also have high drug-loading potential and responsive release after suitable modification with functional compounds, such as MXene [27], which renders them a superior choice for skin disorder management [28–30]. In contrast, regulatory molecules may be therapeutic targets for promoting wound healing. As a representative example, NO signaling with potent antimicrobial, anti-inflammatory, and vasodilation effects exhibited modulatory effects on vascular functions and skin cell activation, thus playing a crucial role in the healing of wounds, which could be possible if the brief half-life and reactive chemical properties of NO are

* Corresponding authors.
   E-mail addresses: entluling60@126.com (L. Lu), fame198288@126.com (W. Sun), yjzhao@seu.edu.cn (Y. Zhao).

Fig. 1. Schematic illustrations of wound healing using near-infrared (NIR)-responsive MNs which encapsulate MXene, gelatin coupled with tert-butyl nitrite (Gel-SNO), and PPBA(pHIF-1α). PPBA: polyamidoamine dendrimer conjugated with phenylboronic acid; pHIF-1α: hypoxia-inducible factor-1α plasmid; TNF-α: tumor necrosis factor-α; IL-6: interleukin-6; CD206: mannose receptor C-type 1; VEGFA: vascular endothelial growth factor A.

effectively managed [31–34]. Additionally, another well-established regulatory factor, HIF-1α, serves as the primary biochemical molecular oxygen detector, influencing cytokine release and genetic activation [35,36]. Specifically, HIF-1α has the capability to induce the release of vascular endothelial growth factor (VEGF), an essential facilitator of angiogenesis, thereby enhancing tissue regeneration [37–39]. Therefore, the composite strategy of integrating NO-donor materials and HIF-1α plasmid with responsive MN technology is promising for diabetic wound treatment.

Herein, we fabricated the desired responsive MNs by using biocompatible MXene gelatin hydrogels for delivering the NO and HIF-1α plasmid to treat the localized diabetic wounds. Due to the incorporation of MXene, the MN patch can rapidly melt, and release NO and HIF-1α plasmid nanoparticles under near-infrared (NIR) irradiation. NO released from gelatin coupled with tert-butyl nitrite (Gel-SNO) achieved potent anti-inflammatory activity *in vitro*. In addition, the HIF-1α plasmid nanoparticles prepared by co-assembled with polyamidoamine dendrimer (PAMAM) conjugated with phenylboronic acid (PBA) (PPBA) could enhance the HIF-1α level in the wound, which triggered the secretion of VEGF and further improved tissue regeneration. Based on these features, the therapeutic effectiveness of the responsive MNs was evaluated in a wound model in diabetic mice. These findings demonstrate that subjects treated with MNs exhibit improved rates of diabetic wound healing, along with heightened anti-inflammatory responses, increased angiogenesis, and enhanced re-epithelialization. Consequently, the MNs featuring controllable release of NO and HIF-1α plasmid display considerable potential for applications in diabetic wound therapy and various other biomedical fields.

2. Materials and methods

2.1. Materials

Gelatin (10 kDa) was purchased from Dalian Meilun Biotechnology Co., Ltd. (China). Generation 5 amine-terminated PAMAM with an ethylenediamine core was obtained from Weihai CY Dendrimer Technology Co., Ltd. (China). Calcein AM, 4′,6-diamidino-2-phenylindole (DAPI), and the Cell Counting Kit-8 (CCK-8) were all purchased from Beyotime, China. Mouse enzyme-linked immunosorbent assay (ELISA) kits were acquired from BioLegend Company in USA. All utilized reagents were of analytical grade.

2.2. Characterization

Stereomicroscopes (SZX16; Olympus, Japan) were used to observe optical and fluorescence photos of MNs and charge coupled devices (DP30BW; Olympus) were used to obtain the images. MNs microstructures were captured by scanning electron microscope (SEM; SU8010; HITACHI, Japan). The fluorescence images were taken by a confocal laser scanning microscope (CLSM; A1; Nikon, Japan). The mechanical strength of MNs by using a displacement force testing system (HP-500; Handpi, China) was tested.

2.3. Cell culture and animals

Human umbilical vein endothelial cells (HUVECs) and RAW 246.7 cells were cultured in Dulbecco's Modified Eagle Medium (DMEM) with high glucose content. All cells were utilized during the logarithmic growth phase, maintained in a culture medium comprising 10% fetal bovine serum and 1% penicillin-streptomycin double antibiotics at 37 °C with 5% CO_2. Male Balb/c mice weighing 20 g and aged 6 to 8 weeks were procured from Nanjing Medical University, China, for the *in vivo* experiments and housed in the Animal Laboratory Center of the Nanjing Drum Tower Hospital (The Affiliated Hospital of Nanjing University Medical School), China. The experimental procedures were authorized by the Animal Care and Use Committee of the Nanjing Drum Tower Hospital, with approval number 2022AE01016 issued by the Laboratory Animal Welfare Ethics Committee of Nanjing Drum Tower Hospital.

2.4. Transfection of hypoxia-inducible factor-1α plasmid (pHIF-1α) in HUVECs

Polyamidoamine dendrimer conjugated with phenylboronic acid (PPBA) was synthesized according to a previously reported method with minor modifications [40]. PPBA(pHIF-1α) was obtained by mixing PPBA and pHIF-1α in a mass ratio of 1:1. The *in vitro* transfection of pHIF-1α by PPBA was evaluated in HUVECs. Lipofectamine 3000 was applied as the positive control, with dosage recommended by the supplier. The cells were seeded on a 12-well plate (1.2×10^5 cells per well) and cultured for 24 h before transfection. PPBA(pHIF-1α) solution (50 μL, 1 mg·mL^{-1} in phosphate-buffered saline (PBS)) was added into each well for further incubation.

2.5. Preparation of Gel-SNO

The solution of gelatin (5 g, 100 mL) was added to 3-mercapto propanyl-N-hydroxysuccinimide ester (2 g) at 50 °C for 12 h. Gel-SH was obtained by dialysis and freeze-drying. Next, tert-butyl nitrite (TBN, 1 g) was added to the methanol/water mixed system (v/v, 1:1) of Gel-SH, and reacted for 24 h at 4 °C. Finally, the unreacted monomer was removed by dialysis, and the Gel-SNO was obtained by freeze-drying.

2.6. Fabrication of the gelatin methacrylate (GelMA)/MXene/Gel-SNO MNs

The tip solution of the MNs was prepared by the combination of GelMA (0.15 g·mL^{-1}), 2-hydroxy-2-methyl propiophenone (HMPP) (1%, v/v), MXene (0.5 mg·mL^{-1}), Gel-SNO (0.05 g·mL^{-1}), and PPBA (pHIF-1α) (100 μg·mL^{-1}). The tip solution (200 μL) was casted into the polydimethylsiloxane (PDMS) mold and centrifuged (4500 r·min^{-1}, 10 min). After removing the excess solution, only the tip was left and the prewarmed gelatin solution at 37 °C was poured into the mold. After illuminating the needle portion with ultraviolet (UV) light (365 nm) for 60 s, the gelatin patch was allowed to cool and cure at room temperature. Eventually, the complete GelMA/MXene/Gel-SNO MNs can be removed.

2.7. Photothermal effect evaluation

The photothermal performance of the GelMA/MXene MNs under 808 nm laser irradiation was assessed using a NIR thermal camera (220s; Fotric, China). Various power densities and concentrations of materials were employed for this evaluation. The real-time temperature of the samples was monitored using a thermocouple probe.

For the assessment of photothermal stability, the GelMA/MXene MNs were exposed to an 808 nm laser until the temperature reached 50 °C, after which the laser was deactivated to allow the sample to cool back to room temperature. The temperatures during both the heating and cooling processes were recorded. This heating-cooling cycle was repeated five times, and the resultant time-temperature curves were plotted to ascertain the photothermal stability of the MNs.

2.8. NIR-controlled NO release property of GelMA/MXene/Gel-SNO MNs

The GelMA/MXene/Gel-SNO MNs underwent continuous irradiation by an 808 nm NIR laser at 1.5 W for a duration of 90 min. The released NO content was measured at 10-min intervals using the Griess assay method. Subsequently, the absorbance of the sample was assessed using a microplate reader to determine the quantity of generated NO. As a control, the NO release profile of the GelMA/MXene/Gel-SNO MNs at room temperature without laser irradiation was utilized for comparison.

2.9. Anti-inflammatory effect in vitro

To evaluate the anti-inflammatory properties of the GelMA/MXene/Gel-SNO MNs, we conducted an experiment using RAW264.7 cells. RAW264.7 cells were placed at a density of 5×10^4 cells per well in the lower chamber of a 24-well transwell plate and treated with 10 μg·mL^{-1} lipopolysaccharide (LPS). The GelMA/MXene/Gel-SNO gel was added to the upper chamber and incubated in the dark for 12 h, followed by 1 h of exposure to NIR light and 11 h in dark. After incubation, the cells were stained with F4/80 (123109; Biolegend, USA), cluster of differentiation 86 (CD86;159203; Biolegend), and mannose receptor C-type 1 (CD206;141707; Biolegend) antibodies and analyzed using confocal laser scanning microscopy. The expression levels of interleukin-6 (IL-6) and tumor necrosis factor-α (TNF-α) were also measured in treated and untreated cells using an ELISA test and a microplate reader.

2.10. Tube formation assay

The tube formation assay was performed by seeding HUVECs into a Matrigel-coated lower chamber in a medium containing 33 mmol·L^{-1} glucose (5×10^4 per well) and 1% O$_2$ for 6 h. The GelMA/MXene/Gel-SNO/PPBA(pHIF-1α) MNs was then added to the upper chamber and incubated in the dark for 12 h. The formation of tubes was evaluated using Calcein-AM staining and imaged under a confocal laser scanning microscope.

2.11. Scratch wound healing assay

In the experimental procedure, HUVECs were subcultured at a density of 1×10^5 cells per well into the lower chamber. Subsequently, the HUVECs were manually scratched using a sterile P200 pipette tip, followed by rinsing with PBS to eliminate any unattached cells. The remaining attached HUVECs were then subjected to treatment with GelMA/MXene/Gel-SNO/PPBA(pHIF-1α) MNs for a duration of 24 h. After the treatment period, the HUVECs were photographed and counted using ImageJ software to evaluate the effects of the MNs treatment on cell migration and proliferation.

2.12. In vivo animal experiment

To produce type I diabetic mice, male Balb/c mice (20 g, 6–8 weeks) were injected intraperitoneally with streptozotocin (100 mg·kg^{-1}). Three days later, the blood glucose levels of each mouse were confirmed. The rats' random blood glucose rose to 11 mmol·L^{-1}, proving that the modeling was successful. Following the shaving of their dorsal regions, a circular, full-thickness cutaneous incision with a diameter of 1 cm was surgically made.

The rats were randomly and equally divided into five groups for the study. Here is a breakdown of each group and the corresponding treatments: control group, GelMA group, GelMA + MXene group, GelMA + MXene + Gel-SNO group, and GelMA + MXene + Gel-SNO + PPBA(pHIF-1α) group. The wounds' development was documented on days 0, 2, 4, 6, 8, and 10. The granulation tissues covering the wound bed were removed and preserved in neutral formaldehyde after all rats were killed on day 10. Following dehydration, the tissue samples were embedded in paraffin and serially sectioned for immunofluorescent labeling, immunohistochemical analysis, and histological examination.

2.13. Statistical analysis

This study's results were all displayed as mean ± standard deviation (SD) ($n \geq 3$). In this paper, every experiment was conducted at least three times. Analysis of variance (ANOVA) or the Student's *t*-test were used to execute and assess statistical differences of the data. A value of $P < 0.05$ was deemed statistically significant.
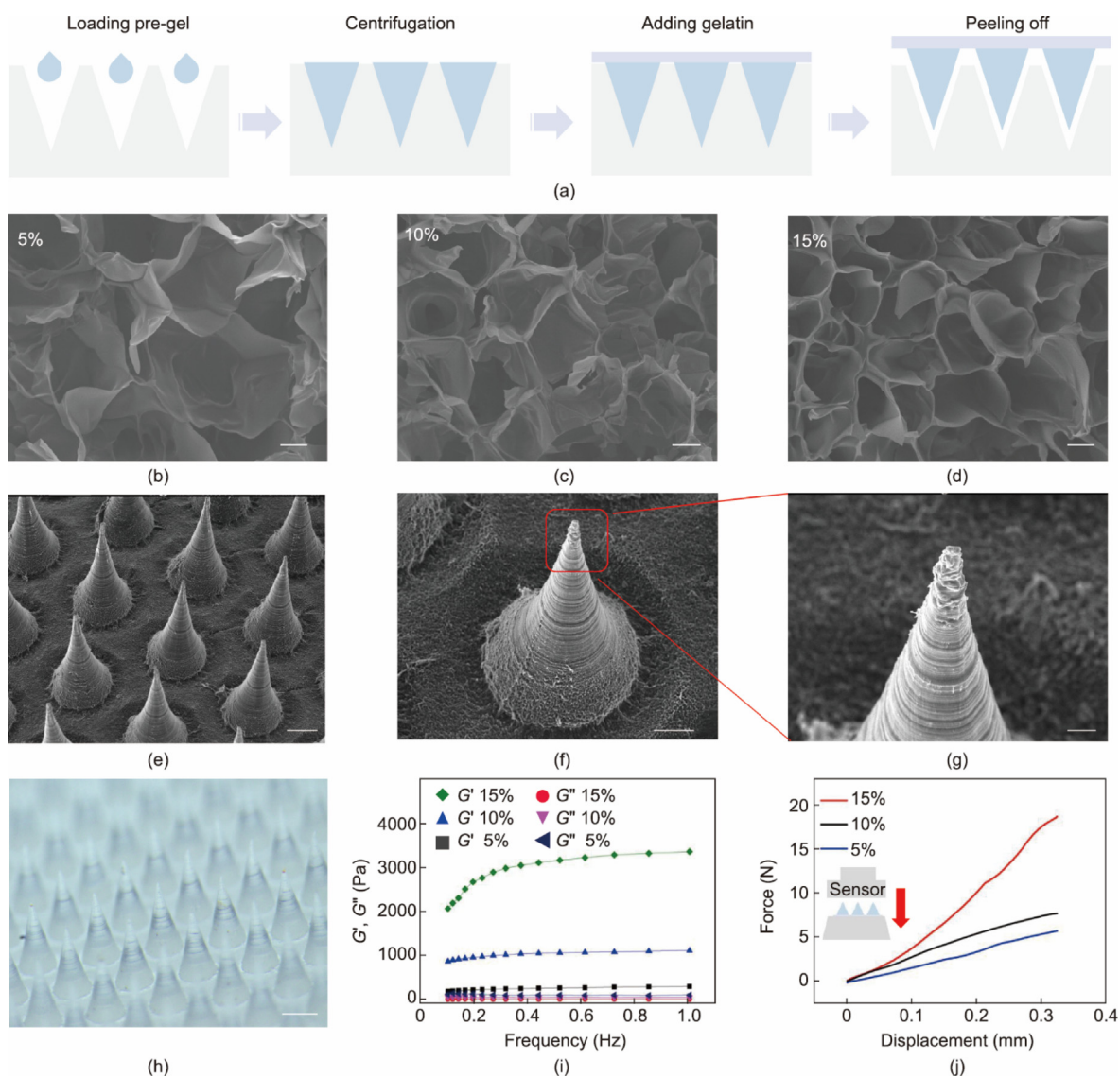
3. Results and discussion

3.1. Fabrication of MNs

To construct thermo-responsive release MNs, Gel-SNO were prepared. Gelatin was selected because of its biocompatibility and biodegradability. To conjugate the NO source to gelatin, the surface groups of gelatin were changed to SNO groups after sulfhydryl reacted with TBN (Fig. S1(a) in Appendix A). The Fourier transform infrared spectroscopy (FTIR) spectrum of Gel-SNO exhibited the characteristic signals of –SNO, implying that Gel-SNO were successfully synthesized (Fig. S1(b) in Appendix A). Further, to

improve the transfect efficiency of pHIF-1α, boronated dendrimer PPBA was synthesized by reacting G5-NH₂ with 4-(bromomethyl) phenylboronic acid according to a previously reported method [40]. To explore the best condition for making pHIF-1α nanoparticles, different weight ratios of PPBA and pHIF-1α were prepared. When the weight ratio between PPBA and pHIF-1α was 1:1, the particle size distribution of PPBA(pHIF-1α) was better and transfection efficiency in HUVECs was the highest (Figs. S2 and S3 in Appendix A). Thus, we kept the weight ratio between PPBA and pHIF-1α as 1:1 in the following study.

In a standard experimental setup, GelMA hydrogel, known for its biocompatibility and bioactive properties, was used as the material for the MNs tips. These MNs incorporated Gel-SNO, PPBA(pHIF-1α), and photoresponsive MXene within their structure. A two-step template replication procedure was used to fabricate the MNs (Fig. 2(a)). After centrifugation, the solution containing the tip material was added to the MNs template. Following the UV polymerization of the needle tips and cooling-induced patch-layer solidification, demolding can be used to produce the required MNs. The GelMA/Gel-SNO hydrogel with porous

Fig. 2. Characterization and mechanical strength of the MNs. (a) A schematic of the MNs arrays manufacturing process. (b–d) SEM images of (b) 5%/5% GelMA/Gel-SNO, (c) 10%/5% GelMA/Gel-SNO, and (d) 15%/5% GelMA/Gel-SNO. Scale bars: 50 μm. (e) SEM photos of the MNs. Scale bar: 200 μm. (f) SEM photos and (g) the enlarged view of the single MN. Scale bars: 100 μm. (h) The optical images of the MNs. Scale bar: 200 μm. (i) Frequency sweep of the GelMA/Gel-SNO hydrogel with different ratio (5%, 10%, and 15%). (j) Mechanical strength of the MNs consisted of GelMA/Gel-SNO with different ratio (5%, 10%, and 15%).

structures was designed to facilitate the release of PPBA(pHIF-1α) through the MNs. SEM images revealed that the pore size of the hydrogel reached up to approximately 50 μm (Figs. 2(b)–(d)). The hydrogel was uniform in optical and SEM images, showing well-organized needle tips (Figs. 2(e)–(h)). The MNs were composed of numerous cones, each measuring 500 μm in base diameter and 600 μm in height. This unique morphology significantly increases the specific surface area, enabling efficient loading of active substances and adequate tissue contact.
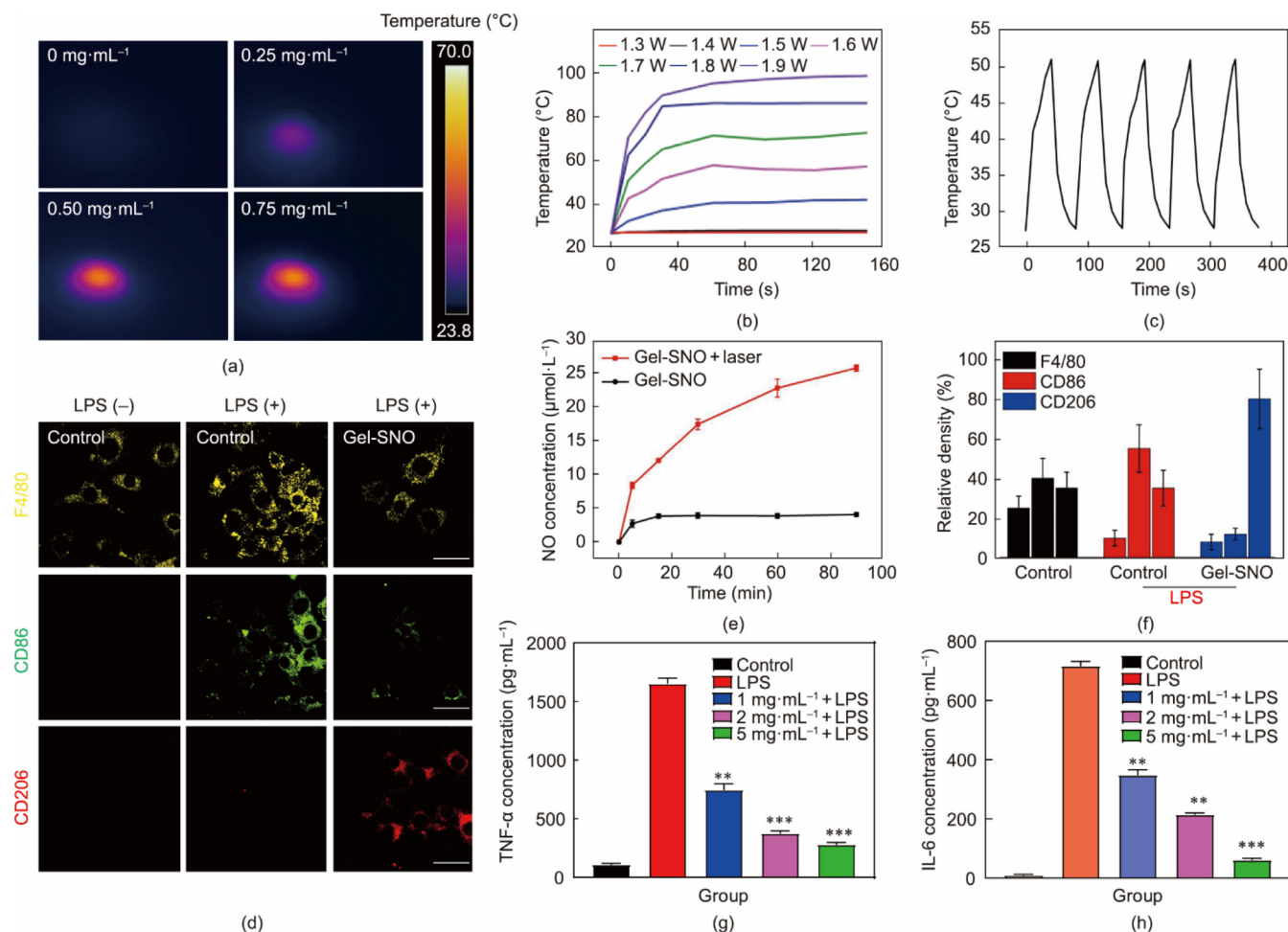
Additionally, the storage modulus (G') of the GelMA/Gel-SNO hydrogel was consistently higher than the loss modulus (G''), which is indicative of normal hydrogel network behavior and guarantees a stable physiological environment for the loaded PPBA (pHIF-1α) (Fig. 2(i)). Mechanical strength testing confirmed that the MNs had sufficient strength to penetrate mouse skin (Fig. 2(j)). The addition of MXene and PPBA(pHIF-1α) did not notably affect the mechanical strength of the Gel-SNO MNs. Moreover, to clarify the targeted delivery of the MNs, we performed tissue staining at the application site. The MNs successfully penetrated the flexible substrate of the wound bed and sufficiently delivered the encapsulated nanoparticles deep into the wound tissue (Fig. S4 in Appendix A). According to the biocompatibility experiments, when co-cultured with MN materials, HUVECs proliferated well, indicating good biocompatibility (Fig. S5 in Appendix A). Considering the mechanical strength and aperture size requirements of the MNs, a

GelMA/Gel-SNO concentration of 15%/5% was selected for subsequent experiments.

3.2. The photothermal performance of MNs

When MNs are exposed to NIR light, the addition of MXenes has the potential to produce heat. When exposed to 1.5 W of NIR light, the temperature of the MNs increased in proportion to the concentration of MXene within 1 min, reaching a peak temperature of approximately 60 °C, as depicted in Fig. 3(a). With an increase in the power of the NIR light source, the temperature of the MNs increased accordingly (Fig. 3(b)). Based on these findings and considering the potential risk of skin burns at higher temperatures, a NIR power of 1.5 W and MXene concentration of 0.5 mg·mL^{-1} were deemed suitable for subsequent experiments. Several photothermal control cycles showed that the prepared MNs exhibited excellent and consistent photothermal performance (Fig. 3(c)). Based on these findings, NIR irradiation may regulate the photoresponsive heating capacity of MNs.

Furthermore, the release of NO from the MNs was examined under 808 nm laser irradiation. The Griess test was used to quantify the amount of NO produced, with a standard curve of NO concentrations obtained for reference (Fig. S6 in Appendix A). As illustrated in Fig. 3(d), it was observed that the triggered release of NO was also achieved upon exposure to 808 nm laser irradiation. Substantial

Fig. 3. Photothermal conversion and controllable NO delivery abilities of the MNs. (a) Thermal images of different concentrations of MXene loaded in the MNs upon 808 nm laser irradiation. (b) Photothermal curves of MXene MNs with different power density irradiated by an 808 nm laser. (c) Temperature changes of MNs during five on/off cycles. The power of NIR light was 1.5 W. (d) Representative images of the M1/M2 level in different groups (n = 3). Scale bars: 20 μm. (e) Laser irradiation (808 nm) triggers NO release. (f) Quantification of the M1/M2 level in different groups from (d) (n = 3). (g, h) Expression of (g) TNF-α and (h) IL-6 in RAW264.7 cells induced by LPS (n = 3) with different concentrations of Gel-SNO. **P < 0.01; ***P < 0.001. Data are presented as mean ± SD (n = 3).

amounts of NO were generated from the MNs under 808 nm laser irradiation, whereas minimal NO release was detected in the non-irradiated samples. These observations collectively demonstrate that MNs can serve as an NO delivery platform for the controlled and precise release of NO through NIR irradiation.
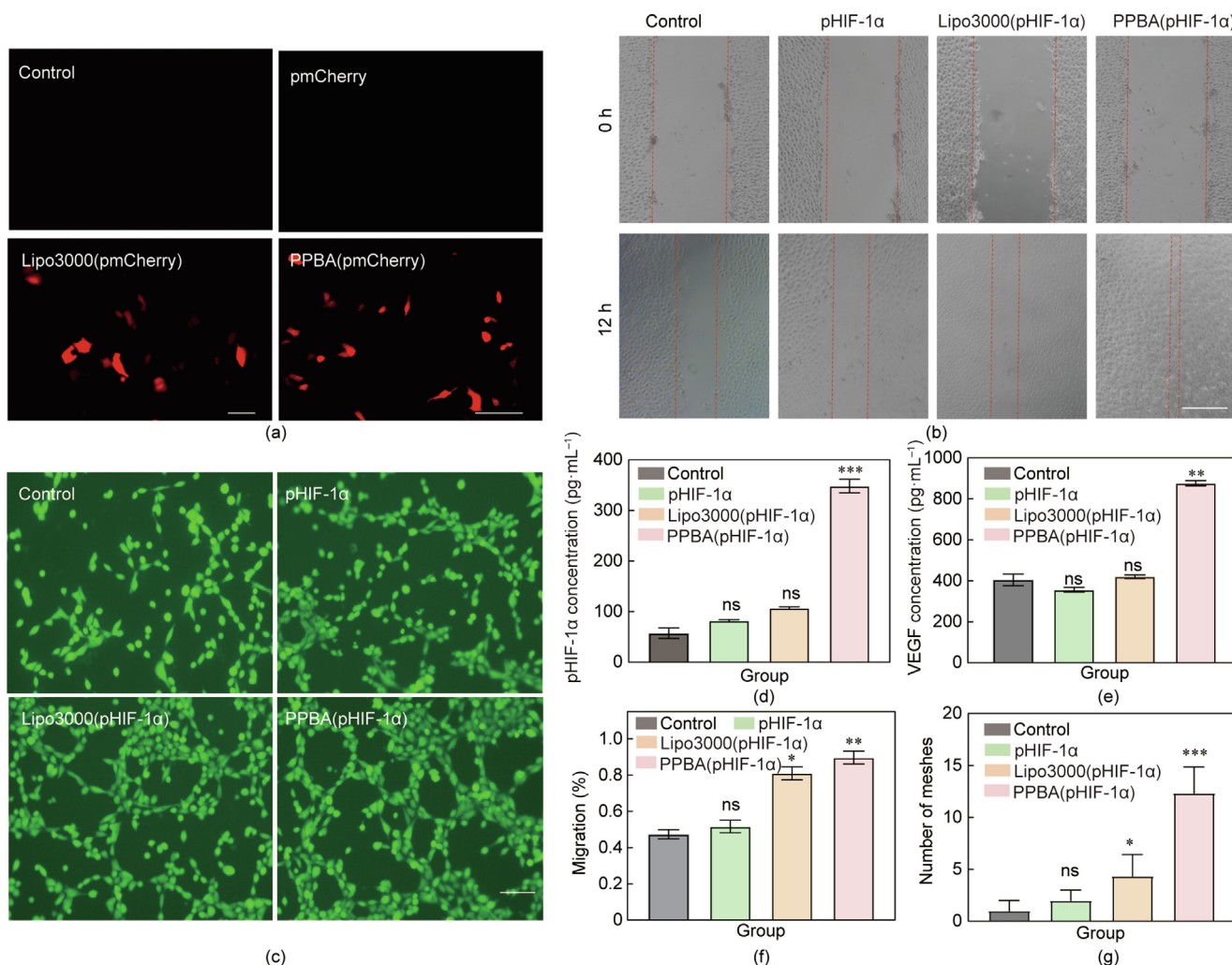
3.3. In vivo therapeutic effects of MNs

Immunostaining analysis showed that MNs were effective in transitioning LPS-stimulated M1 macrophages to M2 macrophages, as evidenced by an increase in CD206 expression and a decrease in CD86 expression (Figs. 3(e) and (f)). Furthermore, based on this observation, the expression of proinflammatory factors (IL-6 and TNF-α) were effectively reduced by the MNs (Figs. 3(g) and (h)). This suggests that the NO released by the MNs helped modulate the macrophage response toward an anti-inflammatory phenotype, thereby promoting a favorable environment for wound healing.

The development of new blood vessels plays a crucial role in providing essential nutrients and oxygen to the wounds, thereby enhancing the speed of wound closure. Therefore, the migration and formation of tubes by HUVECs are vital for angiogenesis. These processes are key determinants of the effectiveness of diabetic wound healing, as they facilitate the establishment of the functional vasculature necessary for tissue repair and regeneration.

To evaluate the effects of the MNs on skin cells in diabetic wounds, in vitro experiments were conducted using HUVECs (Fig. 4). It was hypothesized that enhancing pHIF-1α transfection efficiency would contribute to increased VEGF formation, thereby promoting angiogenesis. We aimed to validate whether PPBA could improve the transfection efficiency of a model plasmid pmCherry compared to that with Lipo3000, which is the current standard for non-viral transfection. As illustrated in Fig. 4(a), the transfection efficiency of PPBA(pmCherry) surpassed that of Lipo3000(pmCherry), indicating its effectiveness in transfection.

Moreover, it was confirmed that the delivery of the pHIF-1α plasmid could promote VEGF production in HUVECs. Figs. 4(d) and (e) showed that the levels of HIF-1α and VEGF in HUVECs were notably higher in the group treated with pHIF-1α, compared with those in other groups. Furthermore, to demonstrate the angiogenesis-promoting ability of PPBA(pHIF-1α), HUVECs were co-cultured with MNs loaded with PPBA(pHIF-1α). The HUVECs formed more visible tubular structures and exhibited a higher number of tubes compared with those of cells without PPBA(pHIF-1α), suggesting that PPBA(pHIF-1α) released from the MNs effectively promoted tube formation (Figs. 4(c) and (g)). Additionally, during the scratch assay, HUVECs cultured in the leaching liquor containing PPBA(pHIF-1α) demonstrated a significantly higher migration rate than that of the control groups, highlighting
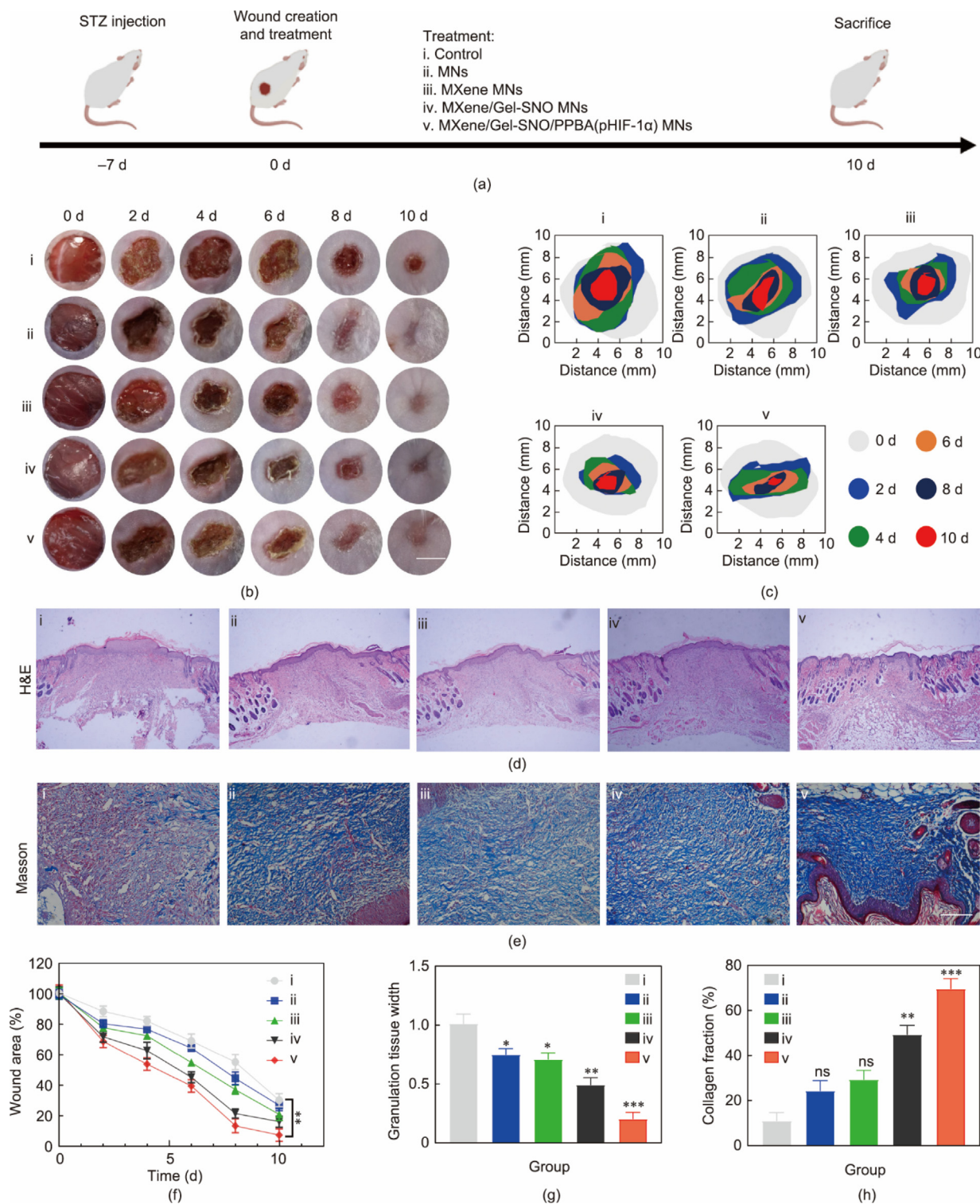

Fig. 4. (a) Representative images of HUVECs transfected with different nanomaterials at 48 h. Scale bars: 50 μm. (b) Representative images of scratch assay of HUVECs treated by PBS, pHIF-1α, Lipo3000(pHIF-1α), and PPBA(pHIF-1α). Scale bar: 200 μm. (c) Representative fluorescent images of the tubule network structure of HUVECs after co-culture with different microcarriers. Scale bar: 100 μm. (d) HIF-1α and (e) VEGF overexpression after transfection with HIF-1α DNA in HUVECs. (f) Quantification of migration rate of HUVECs in (b). (g) Quantitative assessment of the formed tubule. ns, not significant; *P < 0.05; **P < 0.01; ***P < 0.001. Data are presented as mean ± SD (n = 3).

the beneficial effects of PPBA(pHIF-1α)-loaded MNs in promoting cell migration and wound healing (Figs. 4(b) and (f)). These findings collectively suggest the potential of PPBA(pHIF-1α) as a therapeutic agent in enhancing angiogenesis and promoting wound healing in diabetic conditions.

3.4. In vivo wound healing assay of MNs

A diabetic rat model was created with full-thickness cutaneous wounds, and the rats were administered several treatments to evaluate the potential of MNs as a therapy. Fig. 5(a) provides a

Fig. 5. *In vivo* diabetic wound healing evaluation of the MNs. (a) Schematic description of animal experiments treated with (i) PBS, (ii) MNs, (iii) MXene MNs, (iv) MXene/Gel-SNO MNs, and (v) MXene/Gel-SNO/PPBA(pHIF-1α) MNs. (b) Representative photos of diabetic wounds on days 0, 2, 4, 6, 8, and 10. (c) Wound area tracing analysis corresponding to photographs shown in (b). (d) Representative images of H&E staining of the wound areas on day 10. Scale bar: 100 μm. (e) Masson staining images of the diabetic wounds on day 10 with the treatment of different groups. Scale bar: 200 μm. (f) Quantitative analysis of the wound areas. (g) Corresponding quantitative analysis of the granulation tissue width on day 10. (h) Quantitative analysis of collagen positive staining area on day 10. ns, not significant; *$P < 0.05$; **$P < 0.01$; ***$P < 0.001$. Data are presented as mean ± SD ($n = 6$). STZ: streptozotocin.
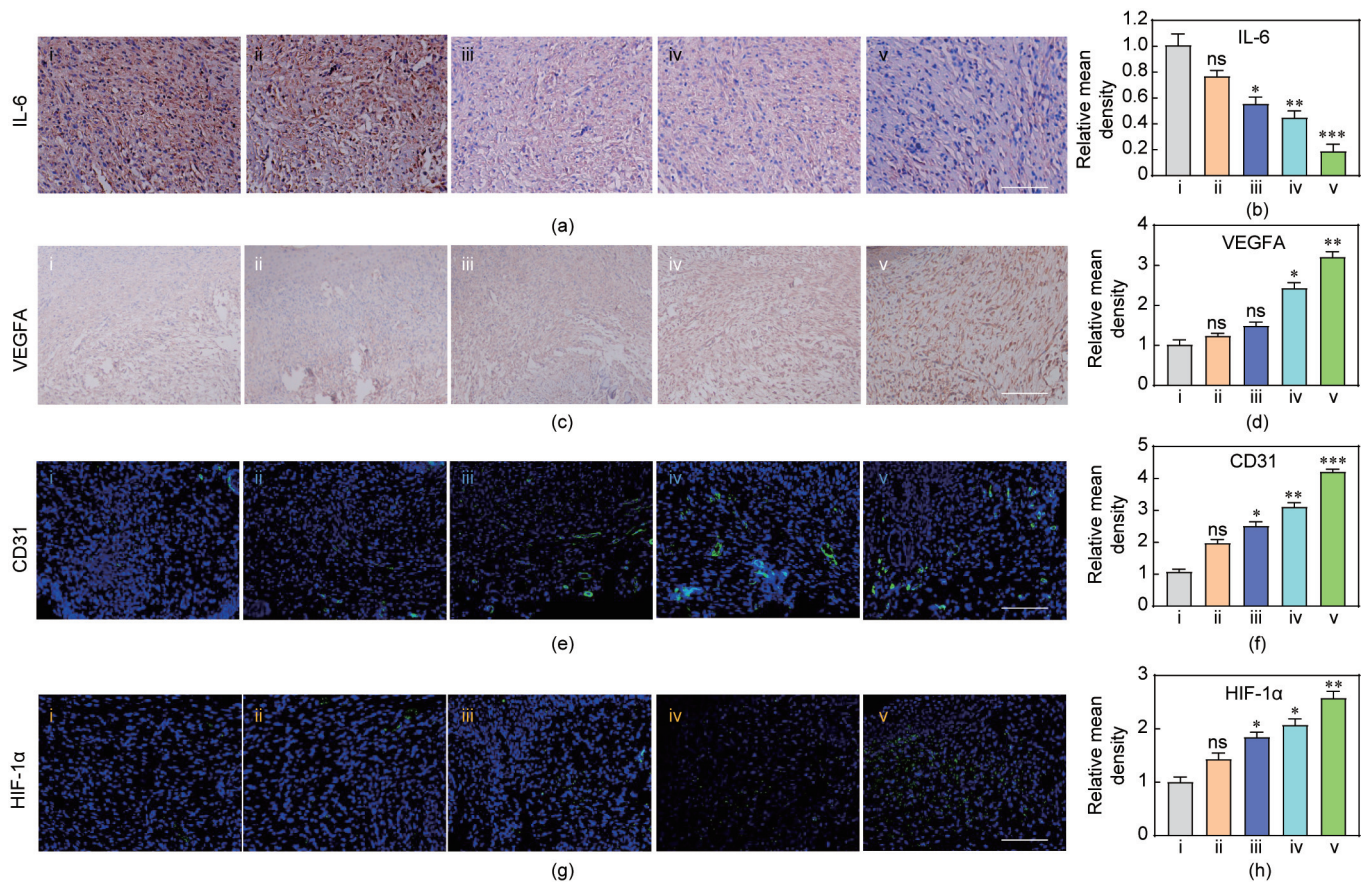
comprehensive history and information on rat grouping. Notably, all rats were hyperglycemic when their blood glucose levels were measured before wound formation. Every two days during the trial, the wounds were photographed and any changes to the wound area were noted. Among all the groups, the rats treated with PPBA(pHIF-1α)-loaded MNs exhibited the most rapid and distinctive reduction in wound area, achieving a wound closure rate of 98% by day 10 (Figs. 5(b) and (c)). The MXene/Gel-SNO MN group also demonstrated significant therapeutic effects; however, it was slightly less effective than the MXene/Gel-SNO/PPBA(pHIF-1α) MN group, which contained pHIF-1α. These findings indicated that the MXene/Gel-SNO/PPBA(pHIF-1α) MN group was more conducive to wound healing compared to other treatment groups. In summary, the results from the diabetic rat model study suggested that the combination of MXene/Gel-SNO/PPBA(pHIF-1α) MNs showed promising potential for promoting wound healing, particularly in diabetic conditions where impaired wound healing is a concern.

3.5. Evaluation of pathological features on wounds

The biological processes by which MNs aid wound healing were examined using histological analysis. Diabetes affects keratinocyte activity and hinders wound healing. Hematoxylin and eosin (H&E) staining was used to assess granulation tissue development and re-epithelialization. When compared with other groups, the MXene/Gel-SNO/PPBA(pHIF-1α) MNs group showed the thickest granulation tissue and most complete stratum corneum, as observed in Fig. 5(d). This suggests that the MXene/Gel-SNO/

PPBA(pHIF-1α) MNs group facilitates the formation of healthy granulation tissues and epithelial layers, which are key components for effective wound healing. Furthermore, following ten days of therapy, histological analysis of the main organs showed no anomalies, suggesting that the MXene/Gel-SNO/PPBA(pHIF-1α) MNs were not harmful to the rats (Fig. S7 in Appendix A). This is an important safety consideration when assessing the applicability of these treatments. Collagen growth and deposition are crucial for wound healing. In comparison to the other groups, the MXene/Gel-SNO/PPBA(pHIF-1α) MNs group showed a more ordered and dense collagen deposition, as shown by Masson's trichrome staining and quantitative analysis. This finding suggests enhanced extracellular matrix reconstruction and tissue remodeling in the presence of MNs, as shown in Fig. 5(e). Further, the corresponding quantitative analysis revealed that the MXene/Gel-SNO/PPBA(pHIF-1α) MNs promoted wound healing, granulation tissue formation, re-epithelialization, and collagen deposition, contributing to improved wound healing outcomes (Figs. 5(f)–(h)). These results highlight the potential of MN-based therapies for enhancing the wound healing process, particularly in diabetic conditions, where impaired wound healing is a significant concern.

A major contributing factor to the pathophysiology of non-healing wounds is chronic inflammation, which is characterized by high levels of proinflammatory cytokines, such as IL-6. According to the study, wounds treated with MXene/Gel-SNO/PPBA(pHIF-1α) MNs had noticeably lower levels of IL-6 than that of wounds treated with other treatment groups, as shown in Figs. 6(a) and (b). This reduction in IL-6 levels suggests that MNs may help to mitigate chronic inflammation, creating a more

Fig. 6. Angiogenesis and inflammation level of diabetic wound model. (a) Corresponding immunohistochemistry staining of IL-6 and (b) quantitative analysis of IL-6 on day 10. (c) Corresponding immunohistochemistry staining of VEGFA and (d) quantitative analysis of VEGFA on day 10. (e) Corresponding immunohistochemistry staining of CD31 and (f) quantitative analysis of CD31 on day 10. (g) Corresponding immunohistochemistry staining of HIF-1α and (h) quantitative analysis of HIF-1α on day 10. The corresponding treatments: (i) PBS, (ii) MNs, (iii) MXene MNs, (iv) MXene/Gel-SNO MNs, and (v) MXene/Gel-SNO/PPBA(pHIF-1α) MNs. Scale bars: 100 μm. ns, not significant; *$P < 0.05$; **$P < 0.01$; ***$P < 0.001$. Data are presented as mean ± SD ($n = 6$).

favorable environment for wound healing. Moreover, the expression of the angiogenic cytokine, VEGFA, was the highest in the MXene/Gel-SNO/PPBA(pHIF-1α) MNs group (Figs. 6(c) and (d)). This indicated that MNs may promote wound healing by enhancing angiogenesis, which is essential for tissue repair and regeneration. CD31 immunofluorescence labeling was used to further examine neovascularization in the wounds. Compared with untreated wounds, wounds treated with MXene/Gel-SNO/PPBA(pHIF-1α) MNs had more neovascularization, as shown by higher fluorescence intensity of CD31 vessels (Figs. 6(e) and (f)). Additionally, staining for HIF-1α revealed higher expression in the MXene/Gel-SNO/PPBA(pHIF-1α) MNs group (Figs. 6(g) and (h)), consistent with the accelerated wound healing observed in this group. These findings suggest that the combination of MXene/Gel-SNO/PPBA(pHIF-1α) MNs could effectively improve angiogenesis, reduce chronic inflammation, and promote wound healing in diabetic wounds. MNs may be crucial in aiding the healing process in difficult situations, such as diabetic wounds, by polarizing monocyte-macrophages toward an anti-inflammatory phenotype and increasing the release of anti-inflammatory cytokines.

4. Conclusions

We developed MXene hydrogel MNs that could release NO and HIF-1α plasmid in a controlled manner, alternating between the delivery of NO and HIF-1α to wounds. The efficacy and biocompatibility of these MNs in treating chronic diabetic wounds were verified through a series of *in vitro* and *in vivo* experiments. The application of MXene/Gel-SNO/PPBA(pHIF-1α) MNs on diabetic wounds led to significant wound closure of 50% by day 5 and 98% re-epithelialization by day 10. Given the challenging non-healing pathological process of diabetic wounds, the potential applications of MXene hydrogel MNs extend beyond diabetic wounds to other types of acute or chronic wounds. The ability of these MNs to promote wound closure and re-epithelialization, reduce inflammation, and enhance tissue regeneration highlights their potential for broader wound-healing applications across various wound types and conditions.

CRediT authorship contribution statement

Wanchuan Ding: Writing – review & editing, Writing – original draft, Validation, Methodology, Investigation. **Xiangyi Wu:** Validation, Methodology, Investigation. **Yi Cheng:** Methodology, Investigation. **Ling Lu:** Supervision, Project administration, Funding acquisition, Conceptualization. **Weijian Sun:** Supervision, Project administration, Funding acquisition, Conceptualization. **Yuanjin Zhao:** Supervision, Project administration, Funding acquisition, Conceptualization.

Declaration of competing interest

The authors declare that they have no known competing financial interests or personal relationships that could have appeared to influence the work reported in this paper.

Acknowledgments

Appendix A. Supplementary data

Supplementary data to this article can be found online at https://doi.org/10.1016/j.eng.2025.06.034.

References

[1] Vartanian A. Diabetic wound dressings. Nat Rev Mater 2024;9:92.
[2] Kang Y, Xu L, Dong J, Yuan X, Ye J, Fan Y, et al. Programmed microalgae-gel promotes chronic wound healing in diabetes. Nat Commun 2024;15:1042.
[3] Wei T, Pan T, Peng X, Zhang M, Guo R, Guo Y, et al. Janus liposozyme for the modulation of redox and immune homeostasis in infected diabetic wounds. Nat Nanotechnol 2024;19:1178–89.
[4] McDermott K, Fang M, Boulton AJM, Selvin E, Hicks CW. Etiology, epidemiology, and disparities in the burden of diabetic foot ulcers. Diabetes Care 2023;46:209–21.
[5] Zhang Y, Wang S, Yang Y, Zhao S, You J, Wang J, et al. Scarless wound healing programmed by core-shell microneedles. Nat Commun 2023;14:3431.
[6] Willenborg S, Sanin DE, Jaiset A, Ding X, Ulas T, Nüchel J, et al. Mitochondrial metabolism coordinates stage-specific repair processes in macrophages during wound healing. Cell Metab 2021;33:2398–414.
[7] Fu X, Wang J, Qian D, Xi L, Chen L, Du Y, et al. Oxygen atom-concentrating short fibrous sponge regulates cellular respiration for wound healing. Adv Fiber Mater 2023;5:1773–87.
[8] Shan J, Che J, Song C, Zhao Y. Emerging antibacterial nanozymes for wound healing. Smart Med 2023;2:e20220025.
[9] Kavanagh F, Rozen W, Seth I, Cuomo R. Exploring the efficacy of negative pressure wound therapy in the management of mycobacterium ulcerans wounds: a comprehensive literature review. Plast Aesthet Res 2024;11:43.
[10] Pignet AL, Hecker A, Voljc T, Carnieletto M, Watzinger N, Kamolz LP. The use of acellular fish skin grafts in burns and complex trauma wounds: a systematic review of clinical data. Plast Aesthet Res 2024;11:40.
[11] Weng W, Wang L, Fan L, Ding X, Wang X. Ordered micro-nano structured biomaterials for wound healing. Biomed Technol 2024;8:104–14.
[12] Song Y, Hu Q, Liu S, Yao G, Zhang H. Electrospinning drug-loaded polycaprolactone/polycaprolactone-gelatin multi-functional bilayer nanofibers composite scaffold for postoperative wound healing of cutaneous squamous cell carcinoma. Biomed Technol 2024;8:65–80.
[13] Chen L, Zhang L, Zhang H, Sun X, Liu D, Zhang J, et al. Programmable immuneactivating electrospun fibers for skin regeneration. Bioact Mater 2021;6:3218–30.
[14] Liu X, Mao X, Ye G, Wang M, Xue K, Zhang Y, et al. Bioinspired *Andrias davidianus* derived wound dressings for localized drug-elution. Bioact Mater 2022;15:482–94.
[15] Shao Z, Yin T, Jiang J, He Y, Xiang T, Zhou S. Wound microenvironment selfadaptive hydrogel with efficient angiogenesis for promoting diabetic wound healing. Bioact Mater 2023;20:561–73.
[16] Sun L, Fan L, Bian F, Chen G, Wang Y, Zhao Y. MXene-integrated microneedle patches with innate molecule encapsulation for wound healing. Research 2021;2021:9838490.
[17] Wang L, Chen G, Fan L, Chen H, Zhao Y, Lu L, et al. Biomimetic enzyme cascade structural color hydrogel microparticles for diabetic wound healing management. Adv Sci 2023;10:2206900.
[18] Zhang X, Li L, Ouyang J, Zhang L, Xue J, Zhang H, et al. Electroactive electrospun nanofibers for tissue engineering. Nano Today 2021;39:101196.
[19] Yu R, Zhang H, Guo B. Conductive biomaterials as bioactive wound dressing for wound healing and skin tissue engineering. Nano-Micro Lett 2022;14:1.
[20] Zhang X, Wang Z, Jiang H, Zeng H, An N, Liu B, et al. Self-powered enzyme-linked microneedle patch for scar-prevention healing of diabetic wounds. Sci Adv 2023;9:eadh1415.
[21] Liu S, Zhang Q, Yu J, Shao N, Lu H, Guo J, et al. Absorbable thioether grafted hyaluronic acid nanofibrous hydrogel for synergistic modulation of inflammation microenvironment to accelerate chronic diabetic wound healing. Adv Healthc Mater 2020;9:e2000198.
[22] Zhu J, Zhou H, Gerhard EM, Zhang S, Rodríguez FIP, Pan T, et al. Smart bioadhesives for wound healing and closure. Bioact Mater 2023;19:360–75.
[23] Ingrole RSJ, Azizoglu E, Dul M, Birchall JC, Gill HS, Prausnitz MR. Trends of microneedle technology in the scientific literature, patents, clinical trials and internet activity. Biomaterials 2021;267:120491.
[24] Cheng R, Liu L, Xiang Y, Lu Y, Deng L, Zhang H, et al. Advanced liposome-loaded scaffolds for therapeutic and tissue engineering applications. Biomaterials 2020;232:119706.
[25] Li L, Zhang X, Zhou J, Zhang L, Xue J, Tao W. Non-invasive thermal therapy for tissue engineering and regenerative medicine. Small 2022;18:e2107705.
[26] Chen B, Zhao Z, Shahbazi MA, Shahbazi MA, Guo X. Microneedle-based technology for cell therapy: current status and future directions. Nanoscale Horiz 2022;7:715.

[27] Huang H, Dong C, Feng W, Wang Y, Huang B, Chen Y. Biomedical engineering of two-dimensional MXenes. Adv Drug Deliv Rev 2022;184:114178.

[28] Zeng Y, Wang C, Lei J, Jiang X, Lei K, Jin Y, et al. Spatiotemporally responsive cascade bilayer microneedles integrating local glucose depletion and sustained nitric oxide release for accelerated diabetic wound healing. Acta Pharm Sin B 2024;14:5037–52.

[29] Wang G, Wang W, Chen Z, Hu T, Tu L, Wang X, et al. Photothermal microneedle patch loaded with antimicrobial peptide/MnO$_2$ hybrid nanoparticles for chronic wound healing. Chem Eng J 2024;482:148938.

[30] Tao H, Xia Y, Tang T, Zhang Y, Qiu S, Chen J, et al. Self-responsive H$_2$-releasing microneedle patch temporally adapts to the sequential microenvironment requirements for optimal diabetic wound healing. Chem Eng J 2024;489:151200.

[31] Yang Z, Chen H, Yang P, Shen X, Hu Y, Cheng Y, et al. Nano-oxygenated hydrogels for locally and permeably hypoxia relieving to heal chronic wounds. Biomaterials 2022;282:121401.

[32] Lundberg JO, Weitzberg E, Gladwin MT. The nitrate–nitrite–nitric oxide pathway in physiology and therapeutics. Nat Rev Drug Discov 2008;7:156–67.

[33] Farah C, Michel LYM, Balligand J. Nitric oxide signalling in cardiovascular health and disease. Nat Rev Cardiol 2018;15:292–316.

[34] Malone-Povolny MJ, Maloney SE, Schoenfisch MH. Nitric oxide therapy for diabetic wound healing. Adv Healthc Mater 2019;8:1801210.

[35] Li G, Ko CN, Li D, Yang C, Wang W, Yang GJ, et al. A small molecule HIF-1α stabilizer that accelerates diabetic wound healing. Nat Commun 2021;12:3363.

[36] Wang Y, Cao Z, Wei Q, Ma K, Hu W, Huang Q, et al. VH298-loaded extracellular vesicles released from gelatin methacryloyl hydrogel facilitate diabetic wound healing by HIF-1α-mediated enhancement of angiogenesis. Acta Biomater 2022;147:342–55.

[37] Cui J, Gong R, Hu S, Cai L, Chen L. Gambogic acid ameliorates diabetes-induced proliferative retinopathy through inhibition of the HIF-1α/VEGF expression via targeting PI3K/AKT pathway. Life Sci 2018;192:293–303.

[38] Zhang D, Lv F, Wang G. Effects of HIF-1α on diabetic retinopathy angiogenesis and VEGF expression. Eur Rev Med Pharmacol Sci 2018;22:5071–6.

[39] Tian M, Li Z, Liu S, Wang Z, Deng B, Cao Y, et al. Ultrasmall copper nanodots eye drops for microenvironment regulation of diabetes retinopathy by relieving hypoxia and inhibiting HIF-1α/VEGF signaling pathway. Chem Eng J 2024;491:152130.

[40] Liu C, Wan T, Wang H, Zhang S, Ping Y, Cheng YA. A boronic acid-rich dendrimer with robust and unprecedented efficiency for cytosolic protein delivery and CRISPR-Cas9 gene editing. Sci Adv 2019;5:eaaw8922.